Title: Development of a Snow Growth Model for Rimed Snowfall

Authors: Ehsan Erfani[1]* and David Mitchell[1]

Affiliation: [1]Desert Research Institute, Reno, Nevada, USA

Corresponding author email: Ehsan.Erfani@dri.edu

Key points:

- A snow growth model was developed that simulates microphysical processes of vapor deposition, aggregation, and riming.

- Lagrangian spiral descent during flight B672 was used to verify the model.

Keywords: ice cloud microphysics, cloud modeling, snow growth model, frontal clouds, cirrus clouds, mixed-phase clouds, aggregation, vapor deposition, riming, particle size distribution

This manuscript is a non-peer reviewed preprint submitted to EarthArXiv.

Development of a Snow Growth Model for Rimed Snowfall

25

Ehsan Erfani[1*]

David Mitchell[1]

[1]Desert Research Institute, Reno, Nevada, USA

Corresponding author email: Ehsan.Erfani@dri.edu

30

Abstract

A snow growth model for rimed snowfall (SGMR) was developed based on the growth processes of vapor deposition, aggregation, and riming. The SGMR is initialized by radar reflectivity (Z) at the cloud top and thereafter simulates the vertical evolution of size spectra.

35 The SGMR is based on the zeroth- and second-moment conservation equations with respect to mass, and thus conserves the number concentration and Z, respectively. New mass- and area-dimension expressions suitable for synoptic clouds are utilized in the model, and therefore the assumption of specific ice particle shapes is not required. In addition, the new approach to parameterizing riming has the advantage of a smooth and gradual growth of mass and area by

40 riming. In general, the processes of vapor deposition and aggregation lead to larger ice particles that fall faster and therefore, produce a larger snowfall rate (r_s). The r_s and ice water content with the inclusion of riming are significantly greater than that produced by the vapor deposition and aggregation alone. Moreover, r_s is sensitive to the cloud drop size distribution. The size spectra predicted by the SGMR were compared with those from two cases of

45 Lagrangian spiral descent through frontal and cirrus clouds, and good agreement is seen between the vertical profiles of SGMR and observations. This analytical SGMR, due to its accuracy and short running time, can be used in climate models and remote sensing.

1 Introduction

50 Since the application of radar to atmospheric science, active and passive remote sensing measurements have added to our understanding of cloud microphysics, but each method has certain drawbacks that impose various limitations with large uncertainties regarding key aspects of cloud microphysics. Moreover, explicitly representing many microphysical processes in large-scale computer models is computationally expensive and thus these

55 processes are parameterized, but with a cost to realism and accuracy. To increase accuracy and reduce computation time, Passarelli (1978a) introduced a simple analytical snow growth model (SGM) that simulated the processes of vapor deposition and aggregation. Due to typical low supercooled liquid water contents (LWC) and weak updrafts (w; for a list of symbols and their definitions, see Appendix A) during winter-time mid-latitude cyclones over USA

60 continental regions, they neglected the effects of riming and w. Moreover, the steady-state and horizontally-homogeneous snowfall assumptions in their model are reasonable for widespread cold stratiform clouds. Their work was followed by several studies (Passarelli, 1978b; Lo, 1983; Mitchell, 1988; 1991; 1994; Field and Heymsfield, 2003; Mitchell et al., 2006).

Many ice cloud microphysical properties can be determined from the ice particle size

65 distribution (PSD). Some studies (Passarelli, 1978a; Lo and Passarelli, 1982; Gordon and Marwitz, 1984) used observational data and derived PSD parameterizations for aggregates. They showed that PSDs often follow an exponential fit for larger particles ($D > 2$ mm). For this reason, early SGMs assumed an exponential PSD shape (Passarelli, 1978b; Lo, 1983; Mitchell, 1988). However, observations by Herzegh and Hobbs (1985) showed that sub-exponential

70 (super-exponential) expressions better fit PSDs in weak stratiform (convective) clouds. Such relationships conform to a gamma distribution:

$$n(D) = N_o D^\nu \exp(-\lambda D),\tag{1}$$

where $n(D)$ is number density, λ is the PSD slope parameter, N_o is the intercept parameter, and ν is the PSD dispersion parameter which is positive (negative) for a sub-exponential (super-exponential) fit (see Fig. 1 in Mitchell, 1994). Note that for exponential PSD, $\nu = 0$. Mitchell

75 (1991) demonstrated the impact of ν on the growth processes of vapor diffusion and

3

aggregation, and Mitchell et al. (2006) found that a super-exponential PSD shape with ν = -0.6 yielded better agreement with the observed PSD height evolution.

Passarelli (1978a), Lo (1983), and Mitchell (1988; 1991; 1994) used moment conservation equations for ice water content (IWC) and radar reflectivity (Z) to predict the evolution of λ and N_o from cloud top to cloud base. They did not use the number concentration (N) moment since they were primarily interested in precipitation development, and the N moment is sensitive to small particles which were not measured adequately at that time. However, a more recent study by Mitchell et al. (2006) employed moment equations for N and Z based on Eq. (1), accounting for both small and large ice particles. Lo (1983) showed a decrease in N_o and λ with a decrease in height, as a result of an increase in particle mean dimension ($\overline{D}$) and a decrease in N with a decrease in height (see Eq. 13). Mitchell (1988) used IWC to initialize an SGM and showed the impact of aggregation on decreasing N. Mitchell (1991) used a profile of snowfall rate r_s (where $r_s = \int V(D)m(D)n(D)dD$, $m(D)$ is ice particle mass and $V(D)$ is particle fallspeed) to initialize the SGM and studied the effect of PSD shape on microphysical characteristics. Their model predicted that super-exponential PSD shape produces the largest ice N followed in order by exponential and sub-exponential PSD shape. This is due to the fact that super-exponential PSD contains relatively high ice particle concentrations that more vigorously compete for water vapor (relative to exponential and sub-exponential PSDs), resulting in relatively narrow PSD. Mitchell et al. (2006) used a vertical profile of relative humidity with respect to ice and a single value of Z at the cloud top as initial conditions. By solving the N and Z moment equations, they predicted vertical profiles of various microphysical variables and showed that $\overline{D}$ (e.g. $\overline{D} = (\nu + 1) / \lambda$ for gamma PSD) increases from cloud top to cloud base as a result of vapor deposition and aggregation growth. The predicted $\overline{D}$ agrees well with observations from an aircraft Lagrangian spiral descent.

An important topic in the SGM calculations is the assumption of aggregation efficiency (E). Unlike the collection efficiency involved with the riming process (for detailed explanations, see Erfani and Mitchell, 2017), E is not well understood. Passarelli (1978b) rearranged the SGM equations and derived a relationship for E that uses various aircraft and Doppler radar measurements. This calculated E had a large scatter and its average was estimated to be 1.4 ±

0.6 for -15 < T < -12. Keith and Saunders (1989) designed an experiment to study the aggregation between planar snow crystals at -11 °C and found that E between a crystal with D = 1 mm and crystals with dimensions of 50, 30, and 20 μm is equal to 0.83, 0.53, and 0.31, respectively. In agreement with this experiment, Mitchell (1988) showed that E should be equal to 0.4 at -20 °C < T < -10 °C, for SGM to predict λ and N accurately. Mitchell et al. (2006) assumed E = 0.07, in agreement with Heymsfield and Kajikawa (1989) as they estimated that E for hexagonal plates in cirrus clouds is between 0.01 and 0.12. Moreover, E can be different based on the selection of moments. By using moment equations for IWC and Z, E is weighted by large particles, whereas by using moment equations for N and Z, E is weighted by smaller particles having fewer extensions and hence lower E values.

In order to calculate the vapor deposition mass growth rate, it is important to account for the effect of the shape factor or dimensionless capacitance (C_s). It is calculated for the spheres, circular disks (as an approximation for hexagonal plates), and needles with an aspect ratio of 5 to be equal to 0.5 (maximum), 0.32, and 0.22, respectively (e.g. Field et al., 2008). For the stationary aggregates (of 3 to 30 component crystals), values of C_s have been calculated theoretically by detecting trajectories of diffusing water molecules (via a random walk approach), and range between 0.25 and 0.28 (Westbrook et al., 2008). This is in agreement with the results of Field et al. (2008) in which they calculated C_s using aircraft observations of a Lagrangian spiral descent in a tropical anvil cloud. C_s calculated by Field et al. (2008) has a mean value of 0.26 and ranges between 0.12 and 0.38.

The computation of ice particle $V(D)$ in a microphysical parameterization is challenging. Most cloud, weather prediction, and climate models use the results of Locatelli and Hobbs (1974) and calculate fallspeed from a V-D power law of the form $V(D) = aD^b$ with constant a and b (e.g. Rutledge and Hobbs, 1984; Ferrier, 1994; Pinski et al., 1998; Morrison and Gettelman, 2008; Gettelman and Morrison, 2015). However, such relationships cannot represent the smooth change in ice particle V as a result of particle growth and consequently produce uncertainty in the microphysical and optical properties of the models. To solve this issue, Mitchell (1996) developed a method that derived V by using ice particle m and A, and also by a Best number (X)-Reynolds number (Re) power law of the form $\mathrm{Re} = A_x X^{B_x}$ (where A_x and B_x

are constant coefficients for a specific range of *X*). In this way, *V* is calculated in terms of its true dependence on the *m/A* ratio. Khvorostyanov and Curry (2002) and Mitchell and Heymsfield (2005) improved this method by using a Re-*X* power law with variable coefficients (A_x and B_x are not constant anymore) to produce a smooth and continuous transition between different flow regimes, and to avoid the discontinuities in *V*. This method represents the evolution of *V* realistically, as is shown by several studies (Morrison and Grabowski, 2008; Morrison and Grabowski, 2010; Jensen and Harrington, 2015; Morrison and Milbrandt, 2015).

2   Methodology

2.1   Model

The model developed in this study is mainly based on Mitchell et al. (2006), but significant improvements are made, including the addition of the riming process to SGM using a new theoretical-empirical method (see Erfani and Mitchell, 2017), changing the traditional *m-D* and *A-D* power laws (e.g., $m = \alpha D^{\beta}$ and $A = \gamma D^{\delta}$, where *α*, *β*, *γ*, and *δ* are constant coefficients) to the new *m-D* and *A-D* power laws with size-dependent coefficients (calculated from *m-D* and *A-D* polynomial curve fits; see Eqs. 4-6 in Erfani and Mitchell, 2016), computing the vapor depositional mass growth rate more accurately (that now includes thermal effects), and calculating the ice fallspeed based on the more accurate method of Mitchell and Heymsfield (2005). Since the SGM in this study includes the riming process, it is now called the snow growth model for rimed snowfall (SGMR).

The rate of change in *n(D)* depends on the model assumptions and also growth processes in the SGM. With the inclusion of vapor deposition, aggregation, and *w*, Passarelli (1978a) and Lo (1983) expressed this rate of change as:

$$\frac{\partial n(m)}{\partial t} = -\frac{\partial}{\partial z}\left\{[w - V(m)]n(m)\right\} - \frac{\partial}{\partial m}\left[\frac{\partial m}{\partial t}n(m)\right]$$

(2)

$$+\frac{1}{2}\int_0^m n(m-m')n(m')k(m-m',m')dm' - n(m)\int_0^\infty n(m')k(m,m')dm' \, .$$

The first term on the right-hand side (RHS) represents the total vertical advection (upward via the updraft and downward via the fallspeed); the second term is the mass growth rate by vapor deposition; the third term is the production of the particle of mass m as a result of collisions between particle of mass m' and particle of mass m-m' with the collection kernel of $k(m-m',m')$ (production by aggregation process); and the fourth term expresses the removal of particles of mass m as a result of its collision with the particle of mass m' (removal by aggregation). The third and fourth terms represent the aggregation process by stochastic (or statistical) collision between ice particles and can be combined into one term via an analytical approach, described in Drake (1972). Although aggregation does not change the total mass of ice particles (e.g. IWC), it changes N, PSD shape, $V(D)$, and $m(D)$.

Similar to Mitchell et al. (2006), our model solves the zeroth moment conservation equation with respect to mass (e.g., moment conservation equation for N) and the second-moment conservation equation with respect to mass (e.g. moment conservation equation for Z). The moment conservation equation for N was calculated by multiplying Eq. (2) by dm and then by integrating over PSD mass. The effect of vapor deposition on the rate of change of N is negligible because it does not produce new particles. The Z moment conservation equation is derived by multiplying Eq. (2) by $m^2 dm$ and then integrating over PSD mass. The resulting equations are:

$$\frac{\partial N}{\partial t} + \frac{\partial(wN - N_f)}{\partial z} = -\frac{1}{2}\int_0^\infty \int_0^\infty n(m)n(m')k(m,m')dmdm' \, , \tag{3}$$

$$\frac{\partial Z}{\partial t} + \frac{\partial(wZ - Z_f)}{\partial z} = 2\int_0^\infty \frac{\partial m}{\partial t}mn(m)dm + \int_0^\infty \int_0^\infty mm'n(m)n(m')k(m,m')dmdm' \, , \tag{4}$$

where wN (wZ) represents the upward flux of N (Z) due to the updraft, and N_f (Z_f) is the downward flux of N (Z) due to particle fallout. The last term on the RHS of both equations represents aggregation that is calculated based on Drake (1972), and the first term on the RHS of Eq. (4) shows vapor deposition. All terms in Eq. (4) can be simplified by using a gamma PSD

from Eq. (1), calculating the integrals using the gamma function definition, and using m-D and V-D power laws. Z_f and N_f are then calculated as:

$$N_f = \int_0^\infty V(D)n(D)dD = \int_0^\infty aD^b N_o D^\nu e^{-\lambda D} dD = \frac{aN_o \Gamma(b+\nu+1)}{\lambda^{b+\nu+1}} \tag{5}$$

$$Z_f = \int_0^\infty V(D)[m(D)]^2 n(D)dD = \int_0^\infty aD^b [\alpha D^\beta]^2 N_o D^\nu e^{-\lambda D} dD = \frac{a\alpha^2 N_o \Gamma(2\beta+b+\nu+1)}{\lambda^{2\beta+b+\nu+1}} \tag{6}$$

Then, the vertical change in N and λ can be derived as:

$$\frac{\partial N}{\partial z} = \frac{bN}{\lambda}\frac{\partial \lambda}{\partial z} + \frac{\Gamma(\nu+1)\lambda^b}{a\Gamma(b+\nu+1)}\left[\frac{\partial(wN)}{\partial z}\right] - \frac{\pi E I(\nu,b)N^2}{8\Gamma(b+\nu+1)\Gamma(\nu+1)\lambda^2}, \tag{7}$$

$$\frac{\partial \lambda}{\partial z} = \left[\frac{a\Gamma(2\beta+b+\nu+1)}{\lambda^b}(2\beta+1)N - 2\beta\Gamma(2\beta+\nu+1)wN\right]^{-1}$$

$$\times \left\{\frac{\partial N}{\partial z}\lambda^{1-b}a\Gamma(2\beta+b+\nu+1) - f(T,P,S)N\lambda^\beta \frac{2\Gamma(\beta+\nu+2)}{\alpha}\right. \tag{8}$$

$$\left. - \frac{\partial(wN)}{\partial z}\lambda\Gamma(2\beta+\nu+1) - \frac{\pi a E I(\beta,\nu,b)N^2}{4\Gamma(\nu+1)\lambda^{b+1}}\right\}$$

where the parameters $I(\nu,b)$ and $I(\beta,\nu,b)$ are integrals that can be solved by Gauss' hypergeometric function. The first term on the RHS of both equations expresses sedimentation and the last term on the RHS of both equations describes aggregation. The second and third terms on the RHS of Eq. (8) are vapor deposition and updraft terms, respectively. The second term on the RHS of Eq. (7) describes the effect of the cloud updraft on the PSD evolution.

The m-D and A-D second-order polynomial fits were used in the SGMR, and they were reduced to power laws (with size-dependent coefficients) for the PSD moment (M_i) and dimension of interest (D_i). This added a few more calculations to the SGMR but made it significantly more realistic. In order to derive N in Eq. (7), all m-D and A-D coefficients are calculated from the median number concentration dimension D_N (for example, $\beta_N = a_1 + 2a_2 \ln D_N$, where a_1 and a_2 are coefficients in m-D polynomial fit and $D_N = (\nu+0.67)/\lambda$; see Eqs. 4-6 in Erfani and

Mitchell, 2016). To derive λ in Eq. (8), the coefficients are calculated from the median radar reflectivity dimension D_Z (e.g. $\beta_Z = a_1 + 2a_2 \ln D_Z$; for the calculation of D_z, see Eq. 10 in Erfani and Mitchell, 2016). To calculate IWC, the coefficients were calculated from the median mass dimension D_m (e.g. $\beta_m = a_1 + 2a_2 \ln D_m$; for the calculation of D_m, see Eq. 7 in Erfani and Mitchell, 2016). This needs an iterative procedure, because β is a function of D_i, and D_i is a function of β. However, only one iteration is sufficient for most applications since the change in D_i is primarily due to the change in λ, and only slightly due to β. An iterative procedure has the following steps: (a) β, δ, α, γ are evaluated at D = 500 μm. (b) D_i is calculated from those coefficients. (c) β, δ, α, γ are recalculated based on D_i and the polynomial curve fit for proper temperature and cloud type. (d) These updated values of coefficients are then used to recalculate D_i.

Using empirical and theoretical methods, Erfani and Mitchell (2017) developed an approach to calculate the change of coefficients in m-D and A-D power laws by riming (Eqs. 6-13 in Erfani and Mitchell, 2017). This parameterization has the benefit of calculating a gradual and smooth growth in m and A. They also calculated the collision efficiency of riming as a function of ice particle size and cloud drop diameter (Eqs. 14-20 in Erfani and Mitchell, 2017). To account for the effect of riming, all these improvements are implemented into the SGMR.

It was assumed by some studies (e.g., Passarelli, 1978a; Mitchell, 1994; Mitchell et al., 2006) that depositional mass growth rate is due only to vapor diffusion (e.g. the thermal effects were neglected). To include the thermal effects, the vapor depositional mass growth rate is now expressed based on an equation from Pruppacher and Klett (1997) to account for both vapor diffusion and thermal effects:

$$\frac{\partial m}{\partial t} = \frac{4\pi C_s D f_v S_{v,i}}{\dfrac{RT_\infty}{e_{sat,i}(T)D_v' M_w} + \dfrac{L_s}{k_a T_\infty}\left(\dfrac{L_s M_w}{RT} - 1\right)} \tag{9}$$

where f_v is ventilation coefficient of water vapor, L_s is specific latent heat of sublimation, $S_{v,i}$ is supersaturation with respect to ice, D_v' is water vapor modified diffusivity, R is universal gas constant, M_w is molecular weight of water (= 18.0160 g mol^{-1}), $e_{sat,i}(T)$ is saturation vapor

pressure over plane ice surface (function of T, only), and k_a is thermal conductivity (for particles larger than 1 µm). Based on Pruppacher and Klett (1997), Gierens et al. (2003), and Harrison et al. (2016), D_v' is calculated as:

$$D_v' = \frac{D_v}{\dfrac{r}{r + \Delta_v} + \dfrac{D_v}{r\alpha_m}\sqrt{\dfrac{2\pi M_w}{RT}}},$$

(10)

where D_v is water vapor normal diffusivity, r is the radius of an equivalent volume sphere, Δ_v is a jump distance (which is equal to molecular mean free path), and α_m is the deposition coefficient. Limited evidence suggested that α_m is ~ 0.01 or less for $D < 100$ µm (Harrison et al., 2016), whereas α_m is greater than 0.1 for $D > 100$ µm (Skrotzki et al., 2013). For more details on calculations of D_v' and α_m, see Gierens et al. (2003) and Harrison et al. (2016). Pruppacher and Klett (1997) expressed an equation for D_v that depends only on environmental conditions:

$$D_v = 0.211\left(\frac{T}{T_0}\right)^{1.94}\left(\frac{P_0}{P}\right),$$

(11)

where D_v is in units of cm^2 sec^{-1}, P is air pressure, T_0 is the freezing temperature of water and P_0 is mean sea-level pressure. They also expressed a relationship for k_a as a function of temperature only:

$$k_a = (5.69 + 0.017T) \times 10^{-5},$$

(12)

where k_a is in units of cal cm^{-1} sec^{-1} °C^{-1} and T is in units of °C. Finally, the shape factor for SGMR is assumed to be 0.25 for aggregates, based on Field et al. (2008) and Westbrook et al. (2008).

2.2   Data

Figure 1 shows the vertical profile of relative humidity with respect to ice (RHi) and liquid water content (LWC) that are used to initialize the SGMR. Based on 36 flights in frontal

stratiform clouds, Korolev and Isaac (2006) provided an equation for RHi as a function of T. Mitchell et al. (2006) modified this equation to avoid RHi < 100 (e.g., sub-saturation conditions). RHi in Fig. 1 is based on the modified equation ($\text{RHi} = 0.0195T^2 + 0.266T + 102.1$) and shows a decrease in RHi from cloud top to cloud base, due to the consumption of water vapor through the formation of new ice particles by nucleation and growth of ice particles by vapor deposition. Profile of LWC is from Mitchell (1995) and is based on measurements at Storm Peak Laboratory (SPL) near Steamboat Springs, Colorado, USA. It shows that LWC is maximized at ~ 600 m above the cloud base, and this is in agreement with the vertical profile of supersaturation with respect to water (see Lamb and Verlinde, 2011, pg. 247 and pg. 435). A sub-exponential gamma distribution was fitted to the cloud droplet PSD from the Isotopic Fractionation in Snow (IFRACS) project, where cloud droplet spectra were measured at SPL during the 2014 winter (for more details, see Borys et al, 2003, and Lowenthal et al., 2011). For this dataset, the median-mass diameter and mean diameter of cloud drops are equal to 15.64 ± 9.79 and 10.19 ± 5.08 μm, respectively.

In order to compare SGMR with observations, aircraft measurements during a Lagrangian spiral descent in a steady-state condition are needed. The first case used in this study is an aircraft descent in a frontal cloud on 8 March 1980 off the coasts of New Hampshire, USA. This case was used by several studies (Lo and Passarelli, 1982; Lo, 1983; Mitchell, 1988; Mitchell et al., 2006) and is referred to as "Spiral 3". For more details on data processing, see those studies. On that date, an aircraft entered a frontal cloud in the warm sector of a cyclone and descended from cloud top (T = -21 ºC) to cloud base (T = -5 ºC) in a Lagrangian spiral path (meteorological conditions are shown in Fig. 2.3 of Lo, 1983). PSD measurements were made by a Particle Measuring System, which is a 1-dimensional laser imaging probe that measures particles in the size range of 200-4500 μm. For this reason, the PSDs are characterized by exponential fits. As explained earlier in Sect. 1, the steady-state assumption is valid in frontal clouds over mid-latitude regions.

The second case study is a Lagrangian spiral descent performed during the night of 30 January 2012 over the Inner Seas off the West Coast of Scotland (started over the south of Vatersay Island, Scotland, and ended over the Kintyre peninsula, Scotland). Hereafter, this case study is

referred to as flight B672. Satellite Infrared (IR) image (figure not shown) shows cirrus clouds over the Atlantic Ocean, Ireland, and northwestern Scotland. Cirrus clouds in the spiral descent are associated with a warm front over the north of Ireland. For a detailed explanation of measurement methods and data processing, see Cotton et al. (2010). A combination of various probes is used to determine ice PSD. Optical array probes (OAP) used in this study are cloud imaging probe (CIP) and 2-dimensional cloud (2DC). Scattering probes are small ice detectors (SID2H, and SID-3) and cloud droplet particles (CDP-15 and CDP-100). CIP-15, CIP-100, and 2DC measure ice particle sizes larger than 60, 400, and 100 μm, respectively. Ice particles larger than 2000 μm are excluded from the calculations, because of the low particle counts in this range. CDP measures ice particle size between 10 and 100 μm, whereas SID2H and SID-3 measure particle size between 10 and 150 μm. The shattering effect of large ice particles was removed by using anti-shatter tips and also by inter-arrival algorithms. The composite PSD is provided from the weighted averaging of the mentioned probes. In order to weigh each probe, counting statistics, uncertainties in sample volumes, and shattering probabilities are taken into account.

3 Results

3.1 General Features of SGMR

Vertical profiles of $\overline{D}$, N and IWC are displayed in Fig. 2 for various combinations of vapor diffusion, aggregation, and riming processes. Overall, it is seen that N ($\overline{D}$) decreases (increases) with a decrease in height. The vapor diffusion process does not change N, but N decreases even when vapor diffusion alone is on, mainly because vapor diffusion leads to the growth of larger particles at lower levels of cloud that fall faster and are removed from the cloud. Compared to vapor diffusion alone, the combination of aggregation and vapor diffusion produces lower N with larger $\overline{D}$. $\overline{D}$ (N) for the combination of aggregation and vapor diffusion is ~ 1.6 times (~ 0.4 times) that for vapor diffusion alone at the cloud base. Because of aggregation, colliding ice crystals stick together and form larger particles. Therefore, aggregation leads to fewer ice particles with larger sizes. The effect of riming on both $\overline{D}$ and

12

N is minimal because the accretion of cloud drops on ice particles does not change the number of ice particles. Also, riming fills in the spaces between branches of ice particles, without changing the maximum dimension. For this reason, $\overline{D}$ and N are rather conserved by riming (for more details, see Erfani and Mitchell, 2017).

The vertical profile of IWC represents an increase from cloud top to cloud base. Vapor diffusion leads to the phase change from vapor to ice, and therefore increases IWC. Aggregation does not change IWC, because it increases the number concentration of larger particles and decreases that of smaller particles without changing the total mass. Riming significantly increases IWC, due to the accretion of cloud drops on the surface of ice particles. With maximum LWC being 0.2 g m^{-3}, riming increases IWC from 0.028 to 0.078 g m^{-3} at cloud base (e.g., rimed IWC becomes $\sim$ 3 times larger than unrimed IWC).

Figure 3 displays the vertical profiles of mass-weighted fallspeed (V_m) and r_s. The r_s is equal to $V_m \times$ IWC, and the size is equal to D_m in order to calculate V_m. Overall, the pattern of V_m shows an increase with a decrease in height, due to an increase in ice particle size, and therefore increase in the m/A ratio. By comparing the condition when aggregation and diffusion exist with the condition that only diffusion exists, it is seen that aggregation leads to larger V_m (by $\sim$ 13% at cloud base) since aggregation causes larger sizes. Riming causes an enhancement of V_m (by $\sim$ 7% at cloud base), because of the formation of more compact ice particles by riming that fall faster. It is seen that rimed particle V_m decreases with a decrease in height near the cloud base because the riming process is shut down at these levels, leading to more branched and less compact particles. The r_s shows a consistent enhancement from cloud top to cloud base, mainly due to changes in IWC. Riming has a significant effect on r_s, and increases r_s by a factor of 2.86. Aggregation, however, has a much smaller impact on r_s because aggregation does not change IWC, but slightly enhances V_m.

3.2 Testing the Riming Process

The simulations of β and α are shown in Fig. 4 for various combinations of vapor diffusion, aggregation, and riming. Unlike many models, β and α are not constant in SGMR, but gradually

13

change as a function of ice particle size (as explained in Erfani and Mitchell, 2016) and rime fraction (as explained in Erfani and Mitchell, 2017). Overall, β decreases from cloud top to cloud base as a result of branching and aggregation. β does not change by riming for a given

325 size. When both aggregation and diffusion are turned on, β is smaller than when only diffusion is turned on. In the absence of riming, α decreases from cloud top to cloud base, due to a decrease in particle density via branching and sticking of ice particles. When both aggregation and diffusion are turned on, α is smaller than when only diffusion is turned on. This is due to the fact that aggregation produces ice particles with large size, but lower density that causes a

330 decrease in α. When riming is turned on, α decreases from the cloud top to the middle of the cloud, but then it increases in agreement with the LWC profile. When cloud droplets accrete on the ice particle surface, they fill in the spaces between the branches, and therefore cause an abrupt increase in density, though particle size is rather conserved. α again starts to decrease with a decrease in height near the cloud base, because the riming process is shut down, and

335 branching and aggregation dominate again. The vertical profiles of γ and δ are similar to α and β, respectively (figures not shown).

Figure 5 represents the vertical profiles of m and A, where m and A are calculated from D_m. The unrimed condition includes vapor diffusion and aggregation processes, whereas the rimed condition includes riming, vapor diffusion, and aggregation. Here, maximum mass (m_{max}) and

340 maximum projected area (A_{max}) refer to the graupel onset mass and projected area, respectively. Unrimed m and A enhance from cloud top to cloud base due to an increase in ice particle size, resulting from the growth of particles by vapor diffusion and aggregation. Rimed m and A are larger than unrimed m and A from the middle of the cloud to the cloud base, as a result of the increase in α by riming (recall that the riming effect on size and β is negligible).

345 At cloud base, rimed m is 2.94 times unrimed m, and rimed A is 2.73 times unrimed A. The results of this section show a gradual and continuous growth from snow crystal to aggregates and graupel that represent the transitional steps of particle growth. Such results are not observed in many climate and cloud models due to the assumption of multiple ice categories and usage of autoconversion from crystals to aggregates and/or from crystals to graupel that

350 occurs instantaneously and is not physical.

3.3 Testing the Aggregation Process

Mitchell (1988) and Mitchell et al. (2006) demonstrated a method to verify the accuracy of the aggregation process in an SGM. The relationship between N_o vs. λ for exponential PSD in log-log space should be linear, and the slope of the regressed line should be close to 2, as verified by Lo and Passarelli (1982), Lo (1983), Mitchell (1988), and Mitchell et al. (2006) for both modeled results and observed data (see Fig. 14 in Mitchell, 1988 and Fig. 9 in Mitchell et al., 2006). A similar relationship is provided in this study (Fig. 6), and it is shown that a linear relationship exists between $\log(N_o)$ and $\log(\lambda)$ for exponential PSD with the slope of the line being equal to 2.2 that agrees well with previous studies, and shows that aggregation process is modeled correctly.

3.4 Implications for Aerosol-Cloud Interaction

Although our SGMR is not initialized by cloud condensation nuclei (CCN), aerosol-cloud interaction can still be tested implicitly in the model. An increase in CCN (due to aerosols) modifies cloud drop size distribution and decreases cloud drop mass-median diameter, when LWC is constant (Twomey et al., 1984). SGMR was run by two different cloud drop PSDs (Fig. 7), and it is seen that smaller cloud drops lead to smaller r_s, and a 50% decrease in the median-mass diameter of cloud drops corresponds to a 30% decrease in r_s at cloud base. The reason for this feature is that smaller drops lead to smaller collision efficiency between ice particles and cloud drops and a smaller riming mass growth rate and thereafter weaken the riming process. Therefore, it is implied that CCNs can suppress the riming growth. Similar results are reported by Zubler et al. (2011) who studied the effect of aerosols in mixed-phase clouds in a numerical prediction model.

3.5   Comparison of Model and Observations

3.5.1 Spiral 3

By analyzing the data from spiral 3, Lo (1983) showed that exponential PSDs (Eq. 1, with $v = 0$) fit well to the data for D > 200 μm (see Fig. 2.7 in Lo, 1983), and from that they calculated N_o and λ as a function of height (see Figs. 2.19 and 2.22 in Lo, 1983). Mitchell et al. (2006) calculated N and $\overline{D}$ for the exponential PSDs using:

$$N = N_o / \lambda \text{ and } \overline{D} = 1/\lambda .$$

(13)

Thereafter, IWC was calculated from:

$$IWC = \int_0^\infty m(D)n(D)dD = \int_0^\infty \alpha D^\beta n(D)dD = \frac{\alpha\Gamma(\beta + v + 1)}{\lambda^{\beta + v + 1}} .$$

(14)

In order to compare the SGMR and observations, exponential PSD was assumed in the first SGMR simulation (e.g., $v = 0$). In addition, another SGMR simulation was performed by assuming super-exponential PSD with $v = -0.6$. In this way, we account for the error of neglecting the small particles.

Figure 8 depicts the vertical profile of $\overline{D}$, N and IWC for observations from Spiral 3, and SGMR for both exponential and super-exponential PSDs. It is seen that SGMR with exponential PSD agrees very well with the observations, and confirms that microphysical characteristics are modeled correctly in the SGMR. Moreover, SGMR with super-exponential PSD shows that ignoring the small ice particles leads to underestimation of N and overestimation of $\overline{D}$, the former being stronger near the cloud top. This is due to the fact that the large number of small particles (as represented by super-exponential PSD) contributes to an increase in the total number of ice particles, and decreases the mean dimension.

16

3.5.2 Flight B672

The observed PSDs were averaged for each complete loop of the Lagrangian spiral, and the results are shown in Fig. 9 for different loops. It is seen that PSDs for this flight are not monomodal, but better conform to bimodal spectra, with a threshold of ~ 200 μm between small and large modes. From cloud top to cloud base, the large-mode $n(D)$ decreases and becomes broader, whereas the small-mode $n(D)$ represents minimal change as a function of height and temperature during Lagrangian descents. The reasons for such features are explained now. 1) It is likely that all levels in the cloud simultaneously experience the ice nucleation process, which is effective for small modes. 2) The small mode contains ice crystals with simple and compact shapes (minimal branching and aggregation) that resist aggregation (e.g. they bounce off other particles upon collision); this tends to preserve their number concentration. However, aggregation is significant for large mode, since large-mode particles are more branched and they more efficiently stick together upon collision. Therefore, the broadening of large-mode $n(D)$ occurs due to aggregation. 3) Small-mode ice crystals fall at speeds ~ 10 cm s^{-1} (see Fig. 6 in Mitchell, 1996, and Fig. 14 in Erfani and Mitchell, 2016), and therefore they remain near the height they were formed for several hours. 4) As explained in Sect. 2.2, α_m ≤ 0.01 for D < 100 μm, but α_m ≥ 0.1 for D > 100 μm; this causes depositional growth of small mode to be at least one order of magnitude slower than that of large mode. The vertical profile of small-mode $\overline{D}$ confirms this since small-mode $\overline{D}$ is rather conserved from cloud top to cloud base (figure not shown).

The SGMR is based on gamma PSD, and therefore, it is needed to parameterize the observed PSDs. For each loop, a gamma function (Eq. 1) is fitted to the small-mode PSD, and another gamma function is fitted to the large-mode PSD, as shown in Fig. 9. The unknown parameters (e.g., v, N_o, and λ) in Eq (1) are calculated from observed N, $\overline{D}$, and D_z, using (Mitchell et al., 2010):

$$v = \frac{\left[(2\beta + 0.67)\overline{D}\right] - D_z}{\overline{D} - D_z} \; , \; \lambda = \frac{v+1}{\overline{D}} \; , \text{ and } \; N_o = \frac{N\lambda^{v+1}}{\Gamma(v+1)} \tag{15}$$

From Fig. 9, it is seen that the fitted gamma PSDs are representative of observed PSDs for the whole size range, with the largest discrepancy for D > 1000 μm. Nonetheless, this does not affect the total number concentration, because $n(D)$ in this size range is more than two orders of magnitude smaller than that for small particles. For example, $n(10 \ \mu m) \sim 1000 \times n(1000 \ \mu m)$. Values of v for both small-mode and large-mode do not depend on temperature or height (figure not shown), and have vertically-averaged values of 1.5 and 8.5, respectively, that are indicative of small-mode and large-mode sub-exponential PSDs.

Due to small changes in small-mode N, $\overline{D}$, and IWC by height, the growth equations in SGMR were solved for large mode, only. In addition, the value of large-mode v in SGMR was assumed to be 8.5 for all levels. Also, the E was assumed to be equal to 0.12 in order to provide the best agreement with observations. Figure 10 shows the vertical profile of N, D_m, and IWC for both SGMR and observation. Although the variability in observations is large, good agreement is seen between SGMR and observations, with SGMR values very close to mean observations for N, D_m, and upper-cloud IWC, and within 1 standard deviation of mean observations for middle- and lower-cloud IWC. All three variables show more sensitivity to the height from the cloud top to the center of the cloud because RHi is larger at the cloud top and decreases with a decrease in height. The effect of aggregation on N seems to be small, because small particles contribute significantly in total N, compared to large particles that are mainly affected by aggregation.

4   Conclusions

Microphysics parameterizations in regional and global models are computationally expensive and produce uncertainties in simulations. Such models mostly use microphysics parameterizations that employ multiple particle categories (such as ice crystal, snowflake, and graupel) and they define an arbitrary threshold for sudden change from ice crystal to aggregates and graupel, which is not realistic and does not occur in the nature. To find solutions for these limitations, an SGMR was developed based on the growth processes of vapor diffusion, aggregation, and riming. The SGMR is capable of simulating the vertical

evolution of the ice PSD by using a measured Z at the cloud top to initialize the SGMR and calculating various microphysical variables at different cloud levels. In this way, it can improve quantitative precipitation estimates, when and where radar observations lack.

The SGMR uses the new method of ice particle A-D and m-D polynomial curve fits introduced by Erfani and Mitchell (2016) that are valid over a much larger size range, compared to traditional power laws. Moreover, the SGMR employs the riming approach suggested by Erfani and Mitchell (2017) to calculate rimed mass and projected area. Therefore, it has the advantage of simulating a continuous and gradual growth from ice crystals to graupel and aggregates, which includes various transitional steps, and there is no need to emphasize an arbitrary and unrealistic autoconversion. SGMR simulations show that from cloud top to cloud base, number concentration decreases due to sedimentation and aggregation, whereas the mean dimension increases by vapor diffusion and aggregation, which leads to an increase in fallspeed. In addition, an increase in IWC corresponds to the enhancement of the snowfall rate. SGMR results show that although riming often has a minor impact on ice particle size, its effect on ice particle mass and projected area is considerable. The riming process is essential in characterizing the ice water content and snowfall rates, with snowfall rates often a factor of three greater than those produced by vapor deposition and aggregation alone. Moreover, a decrease in the median-mass diameter of cloud drops (caused by an increase in aerosols or CCN), decreases the collision efficiency of riming and the riming mass growth rate, which leads to a decrease in the snowfall rate.

The size spectra predicted by the SGMR are in good agreement with the observed spectra from aircraft measurement during Lagrangian spiral descents through a frontal cloud on 8 March 1980 off the coasts of New Hampshire, U.S.A., and through cirrus clouds on 30 January 2012 over the Inner Seas off the West Coast of Scotland. The PSDs from the latter show the bimodal spectra that indicate different microphysical processes for small and large modes. The agreements between the model and observations show that microphysical characteristics are simulated accurately in the model. By using only one category of ice particle in SGMR, its running time is significantly less than the models with multiple categories of particles. Since

SGMR is an analytical model, it is accurate and computationally efficient, and therefore it can be beneficial in the improvement of climate models.

Appendix A: List of symbols

a prefactor in fall speed-dimension power law

a_o, a_1, a_2 coefficient in *m-D* polynomial expression

A projected area

A_{max} graupel projected area

A_x prefactor in Reynolds number-Best number power law

b exponent in fall speed-dimension power law

B_x exponent in Reynolds number-Best number power law

C_s shape factor

D maximum dimension of ice particle

$\overline{D}$ mean maximum dimension of a PSD

D_i dimension of interest

	D_m	median mass dimension
505	D_N	number concentration dimension
	D_v	water vapor normal diffusivity
	$D_v^{'}$	water vapor modified diffusivity
	D_Z	reflectivity dimension
	$e_{sat,i}$	saturation vapor pressure over plane ice surface
510	E	aggregation efficiency
	f_v	ventilation coefficient of water vapor
	I	integral solved by Gauss' hypergeometric function
	k	collection kernel
	k_a	thermal conductivity
515	L_s	specific latent heat of sublimation
	m	mass of ice particle
	m_{max}	graupel mass
	M_w	molecular weight of water
	n	number density
520	N	number concentration
	N_f	downward flux of radar reflectivity
	N_o	intercept parameter of a gamma PSD
	P	air pressure
	r	radius of an equivalent volume sphere
525	r_s	snowfall rate
	R	universal gas constant
	Re	Reynolds number
	$S_{v,i}$	supersaturation with respect to ice
	t	time
530	T	temperature
	V	terminal fallspeed of ice particle
	V_m	mass-weighted terminal fallspeed
	w	updraft

X		Best number
z		height
Z		radar reflectivity
Z_f		downward flux of radar reflectivity
α		prefactor in mass-dimension power law
α_m		deposition coefficient
β		exponent in mass-dimension power law
γ		prefactor in projected area-dimension power law
δ		exponent in projected area-dimension power law
Δ_v		jump distance
Γ		gamma function
λ		slope parameter of a gamma PSD
ν		dispersion parameter of a gamma PSD

535 z height

540 β exponent in mass-dimension power law

545 λ slope parameter of a gamma PSD

References

Borys, R. D., Lowenthal, D. H., Cohn, S. A., and Brown, W. O. J.: Mountaintop and radar measurements of
550   anthropogenic aerosol effects on snow growth and snowfall rate, 30,
https://doi.org/10.1029/2002gl016855, 2003.

Cotton, R., Osborne, S., Ulanowski, Z., Hirst, E., Kaye, P. H., and Greenaway, R. S.: The Ability of the Small Ice
Detector (SID-2) to Characterize Cloud Particle and Aerosol Morphologies Obtained during Flights of the
FAAM BAe-146 Research Aircraft, J. Atmos. Oceanic Tech., 27, 290–303,
555   https://doi.org/10.1175/2009jtecha1282.1, 2010.

Drake, R. L.: The Scalar Transport Equation of Coalescence Theory: Moments and Kernels, J. Atmos. Sci., 29,
537–537, https://doi.org/10.1175/1520-0469(1972)029<0537:TSTEOC>2.0.CO;2, 1972.

Erfani, E. and Mitchell, D. L.: Developing and bounding ice particle mass- and area-dimension expressions for
use in atmospheric models and remote sensing, Atmos. Chem. Phys., 16, 4379–4400,
560   https://doi.org/10.5194/acp-16-4379-2016, 2016.

Erfani, E. and Mitchell, D. L.: Growth of ice particle mass and projected area during riming, Atmospheric
Chemistry and Physics, 17, 1241–1257, https://doi.org/10.5194/acp-17-1241-2017, 2017.

Facility for Airborne Atmospheric Measurements; Natural Environment Research Council; Met Office: FAAM
B672 PIKNMIX flight, number 8: Airborne atmospheric measurements from core instrument suite on board
565   the BAE-146 aircraft, NCAS British Atmospheric Data Centre, [dataset],

https://catalogue.ceda.ac.uk/uuid/e4ffe30f47fa41c18f2241905a51f7c1, Accessed 31 Mar 2024, 2014.

Ferrier, B. S.: A Double-Moment Multiple-Phase Four-Class Bulk Ice Scheme. Part I: Description, J. Atmos. Sci., 51, 249–280, 1994.

Field, P. R. and Heymsfield, A. J.: Aggregation and scaling of ice crystal size distributions, J. Atmos. Sci., 60, 544–560, https://doi.org/10.1175/1520-0469(2003)060<0544:aasoic>2.0.co;2, 2003.

Field, P. R., Heymsfield, A. J., Bansemer, A., and Twohy, C. H.: Determination of the combined ventilation factor and capacitance for ice crystal aggregates from airborne observations in a tropical anvil cloud, J. Atmos. Sci., 65, 376–391, https://doi.org/10.1175/2007jas2391.1, 2008.

Gettelman, A. and Morrison, H.: Advanced Two-Moment Bulk Microphysics for Global Models. Part I: Off-Line Tests and Comparison with Other Schemes, J. Clim., 28, 1268–1287, https://doi.org/10.1175/jcli-d-14-00102.1, 2015.

Gierens, K. M., Monier, M., and Gayet, J. F.: The deposition coefficient and its role for cirrus clouds, J. Geophys. Res.-Atmos., 108, https://doi.org/10.1029/2001jd001558, 2003.

Gordon, G. L. and Marwitz, J. D.: An Airborne Comparison of Three PMS Probes, J. Atmos. Oceanic Tech., 1, 22–27, https://doi.org/10.1175/1520-0426(1984)001<0022:AACOTP>2.0.CO;2, 1984.

Harrison, A., Moyle, A. M., Hanson, M., and Harrington, J. Y.: Levitation Diffusion Chamber Measurements of the Mass Growth of Small Ice Crystals from Vapor, J. Atmos. Sci., 73, 2743–2758, https://doi.org/10.1175/jas-d-15-0234.1, 2016.

Herzegh, P. H. and Hobbs, P. V.: Size spectra of ice particles in frontal clouds: correlations between spectrum shape and cloud conditions, Q. J. Roy. Meteor. Soc., 111, 463–477, https://doi.org/10.1256/smsqj.46809, 1985.

Heymsfield, A. J. and Kajikawa, M.: Aggregation of ice crystals in cirrus, J. Atmos. Sci., 46, 3108–3121, 1989.

Isotopic Fractionation in Snow: GAUS Radiosonde Data. Version 1.0., UCAR/NCAR - Earth Observing Laboratory, [dataset], https://doi.org/10.5065/D6988568. Accessed 31 Mar 2024, 2014.

Jensen, A. A. and Harrington, J. Y.: Modeling Ice Crystal Aspect Ratio Evolution during Riming: A Single-Particle Growth Model, J. Atmos. Sci., 72, 2569–2590, https://doi.org/10.1175/jas-d-14-0297.1, 2015.

Keith, W. D. and Saunders, C. P. R.: The collection efficiency of a cylindrical target for ice crystals, Atmos. Res., 23, 83–95, https://doi.org/10.1016/0169-8095(89)90059-8, 1989.

Khvorostyanov, V. I. and Curry, J. A.: Terminal velocities of droplets and crystals: Power laws with continuous parameters over the size spectrum, J. Atmos. Sci., 59, 1872–1884, https://doi.org/10.1175/1520-0469(2002)059<1872:TVODAC>2.0.CO;2, 2002.

Korolev, A. and Isaac, G. A.: Relative Humidity in Liquid, Mixed-Phase, and Ice Clouds, J. Atmos. Sci., 63, 2865–2880, https://doi.org/10.1175/JAS3784.1, 2006.

Lamb, D. and Verlinde, J.: Physics and Chemistry of Clouds, Cambridge University Press, New York, NY, USA, 2011.

Lo, K. K.: growth process of snow, Report No. AFGL-TR-83-0105, 192 pp, 1983.

Lo, K. K. and Passarelli, R. E.: The Growth of Snow in Winter Storms: An Airborne Observational Study, J. Atmos.

Sci., 39, 697–706, https://doi.org/10.1175/1520-0469(1982)039<0697:tgosiw>2.0.co;2, 1982.

Locatelli, J. d. and Hobbs, P. V.: Fall speeds and masses of solid precipitation particles, J. Geophys. Res., 79, 2185–

605   2197, https://doi.org/10.1029/JC079i015p02185, 1974.

Lowenthal, D. H., Borys, R. D., Cotton, W., Saleeby, S., Cohn, S. A., and Brown, W. O. J.: The altitude of snow

growth by riming and vapor deposition in mixed-phase orographic clouds, Atmos. Environ., 45, 519–522,

https://doi.org/10.1016/j.atmosenv.2010.09.061, 2011.

Mitchell, D. L.: Evolution of snow-size spectra in cyclonic storms .1. snow growth by vapor-deposition and

610   aggregation, J. Atmos. Sci., 45, 3431–3452, https://doi.org/10.1175/1520-

0469(1988)045<3431:eosssi>2.0.co;2, 1988.

Mitchell, D. L.: Evolution of snow-size spectra in cyclonic storms .2. deviations from the exponential form, J.

Atmos. Sci., 48, 1885–1899, https://doi.org/10.1175/1520-0469(1991)048<1885:eosssi>2.0.co;2, 1991.

Mitchell, D. L.: A model predicting the evolution of ice particle size spectra and radiative properties of cirrus

615   clouds. Part I: Microphysics, J. Atmos. Sci., 51, 797–816, https://doi.org/10.1175/1520-

0469(1994)051<0797:AMPTEO>2.0.CO;2, 1994.

Mitchell, D. L.: An analytical model predicting the evolution of ice particle size distributions, University of

Nevada-Reno, PhD Dissertation, 181 pp., 1995.

Mitchell, D. L.: Use of mass- and area-dimensional power laws for determining precipitation particle terminal

620   velocities, J. Atmos. Sci., 53, 1710–1723, https://doi.org/10.1175/1520-

0469(1996)053<1710:uomaad>2.0.co;2, 1996.

Mitchell, D. L. and Heymsfield, A. J.: Refinements in the treatment of ice particle terminal velocities, highlighting

aggregates, J. Atmos. Sci., 62, 1637–1644, https://doi.org/10.1175/jas3413.1, 2005.

Mitchell, D. L., Huggins, A., and Grubisic, V.: A new snow growth model with application to radar precipitation

625   estimates, Atmos. Res., 82, 2–18, https://doi.org/10.1016/j.atmosres.2005.12.004, 2006.

Mitchell, D. L., d'Entremont, R. P., and Lawson, R. P.: Inferring Cirrus Size Distributions through Satellite Remote

Sensing and Microphysical Databases, J. Atmos. Sci., 67, 1106–1125,

https://doi.org/10.1175/2009jas3150.1, 2010.

Morrison, H. and Gettelman, A.: A new two-moment bulk stratiform cloud microphysics scheme in the

630   community atmosphere model, version 3 (CAM3). Part I: Description and numerical tests, J. Clim., 21, 3642–

3659, https://doi.org/10.1175/2008jcli2105.1, 2008.

Morrison, H. and Grabowski, W. W.: A novel approach for representing ice microphysics in models: Description

and tests using a kinematic framework, J. Atmos. Sci., 65, 1528–1548,

https://doi.org/10.1175/2007jas2491.1, 2008.

635   Morrison, H. and Grabowski, W. W.: An Improved Representation of Rimed Snow and Conversion to Graupel in

a Multicomponent Bin Microphysics Scheme, J. Atmos. Sci., 67, 1337–1360,

https://doi.org/10.1175/2010jas3250.1, 2010.

Morrison, H. and Milbrandt, J. A.: Parameterization of Cloud Microphysics Based on the Prediction of Bulk Ice

Particle Properties. Part I: Scheme Description and Idealized Tests, J. Atmos. Sci., 72, 287–311,

640   https://doi.org/10.1175/jas-d-14-0065.1, 2015.

Passarelli, R. E.: Theoretical and Observational Study of Snow-Size Spectra and Snowflake Aggregation
Efficiencies, J. Atmos. Sci., 35, 882–889, https://doi.org/10.1175/1520-
0469(1978)035<0882:taosos>2.0.co;2, 1978a.

Passarelli, R. E., Jr.: Approximate analytical model of the vapor deposition and aggregation growth of

645   snowflakes, J. Atmos. Sci., 35, 118–124, https://doi.org/10.1175/1520-
0469(1978)035<0118:AAAMOT>2.0.CO;2, 1978b.

Pinsky, M., Khain, A., Rosenfeld, D., and Pokrovsky, A.: Comparison of collision velocity differences of drops and
graupel particles in a very turbulent cloud, Atmos. Res., 49, 99–113, https://doi.org/10.1016/s0169-
8095(98)00073-8, 1998.

650 Pruppacher, H. R. and Klett, J. D.: Microphysics of clouds and precipitation: 2nd edn, Kluwer Academic
Publishers, Dordrecht, the Netherlands, 1997.

Rutledge, S. A. and Hobbs, P. V.: The Mesoscale and Microscale Structure and Organization of Clouds and
Precipitation in Midlatitude Cyclones. XII: A Diagnostic Modeling Study of Precipitation Development in
Narrow Cold-Frontal Rainbands, J. Atmos. Sci., 41, 2949–2972, https://doi.org/10.1175/1520-

655   0469(1984)041<2949:tmamsa>2.0.co;2, 1984.

Skrotzki, J., Connolly, P., Schnaiter, M., Saathoff, H., Möhler, O., Wagner, R., Niemand, M., Ebert, V., and Leisner, T.:
The accommodation coefficient of water molecules on ice - cirrus cloud studies at the AIDA simulation
chamber, Atmos. Chem. Phys., 13, 4451–4466, https://doi.org/10.5194/acp-13-4451-2013, 2013.

Twomey, S. A., Piepgrass, M., and Wolfe, T. L.: An assessment of the impact of pollution on global cloud albedo,

660 Tellus, 36B, 356–366, https://doi.org/10.1111/j.1600-0889.1984.tb00254.x, 1984.

Westbrook, C. D., Hogan, R. J., and Illingworth, A. J.: The capacitance of pristine ice crystals and aggregate
snowflakes, J. Atmos. Sci., 65, 206–219, https://doi.org/10.1175/2007jas2315.1, 2008.

Zubler, E. M., Lohmann, U., Lüthi, D., Schär, C., and Muhlbauer, A.: Statistical Analysis of Aerosol Effects on
Simulated Mixed-Phase Clouds and Precipitation in the Alps, J. Atmos. Sci., 68, 1474,

665 https://doi.org/10.1175/2011JAS3632.1, 2011.

Figure Captions

Figure 1. Vertical profile of liquid water content and relative humidity with respect to ice.

Figure 2. Vertical profile of (a) mean dimension, (b) number concentration, and (c) ice water content for various combinations of vapor diffusion, aggregation, and riming processes.

Figure 3. Same as Fig. 2, but for (a) mass-weighted fallspeed and (b) snowfall rate.

Figure 4. Same as Fig. 3, but for (a) β and (b) α.

Figure 5. Vertical profile of (a) projected area and (b) mass calculated from median-mass dimension for rimed, unrimed, and graupel onset conditions (maximum mass and area refer to the graupel onset).

Figure 6. log(No) vs. log(λ) for exponential PSD. Each circle shows a vertical level in the modeled cloud with a vertical distance of 180 m to the upper or lower level. The cloud top is represented by the uppermost circle.

Figure 7. Vertical profile of snowfall rate for two liquid cloud PSDs: The blue curve corresponds to the drop median-mass diameter being equal to 10 μm, and the red curve represents the drop median-mass diameter being equal to 20 μm.

Figure 8. Vertical profile of (a) mean dimension and (b) number concentration for observation, model with super-exponential PSD, and model with exponential PSD. (c) Vertical profile of IWC for observation and model with exponential PSD.

Figure 9. Observed PSD (blue circles) and bimodal gamma PSD (black curves) fitted to the observed PSD. Observed PSD in each panel is provided by averaging a complete loop of the Lagrangian spiral. Observations are from flight B672.

Figure 10. Vertical profile of (a) median-mass dimension, (b) number concentration, and (c) ice water content for observation, model with diffusion and aggregation processes, and model with diffusion process. Each blue circle (horizontal line) is the mean (standard deviation) of a complete loop of the Lagrangian spiral. Observations are from flight B672.
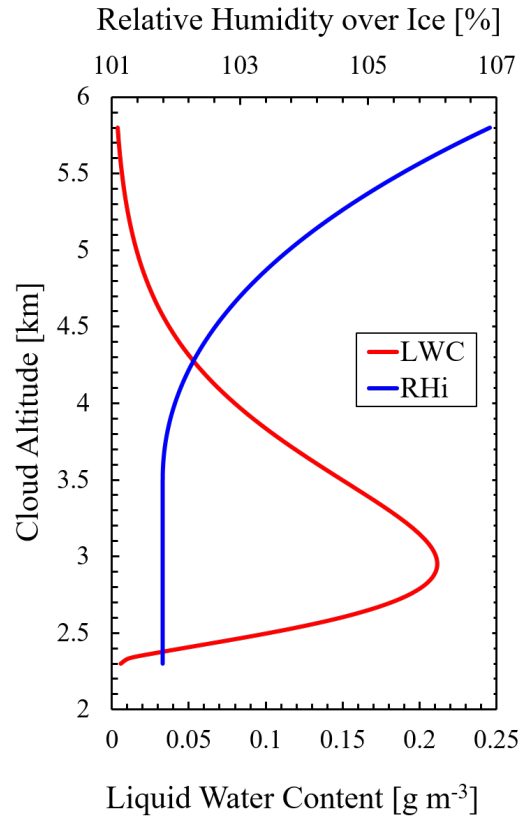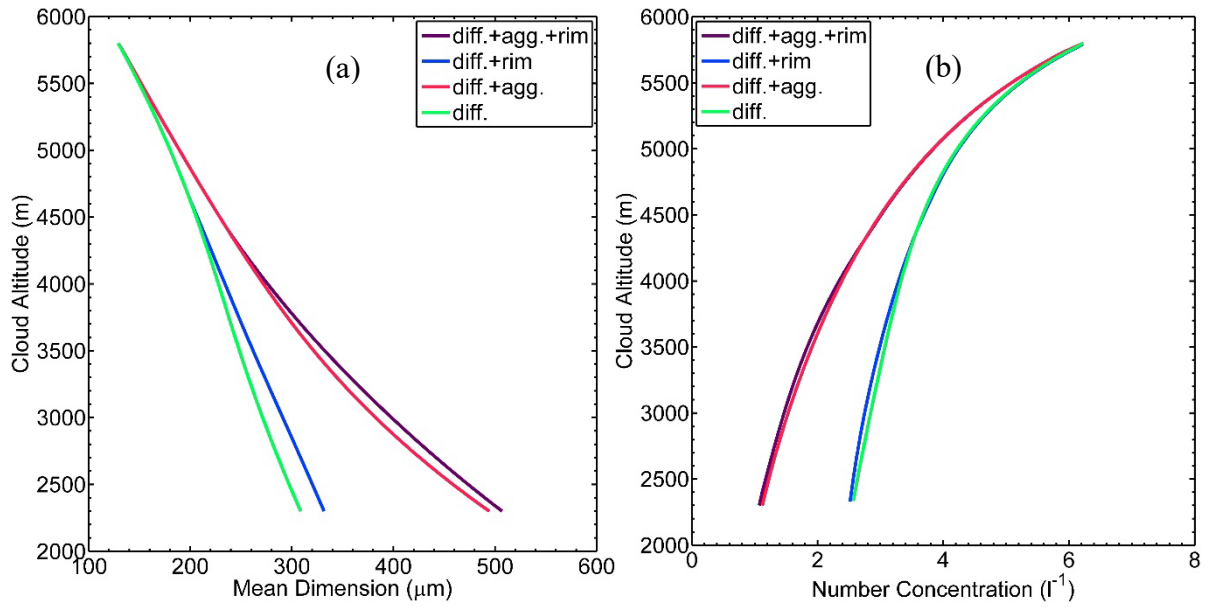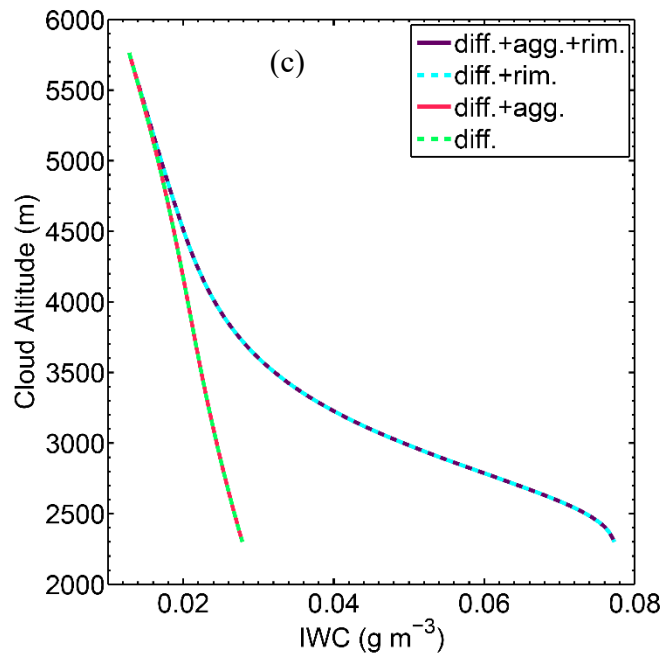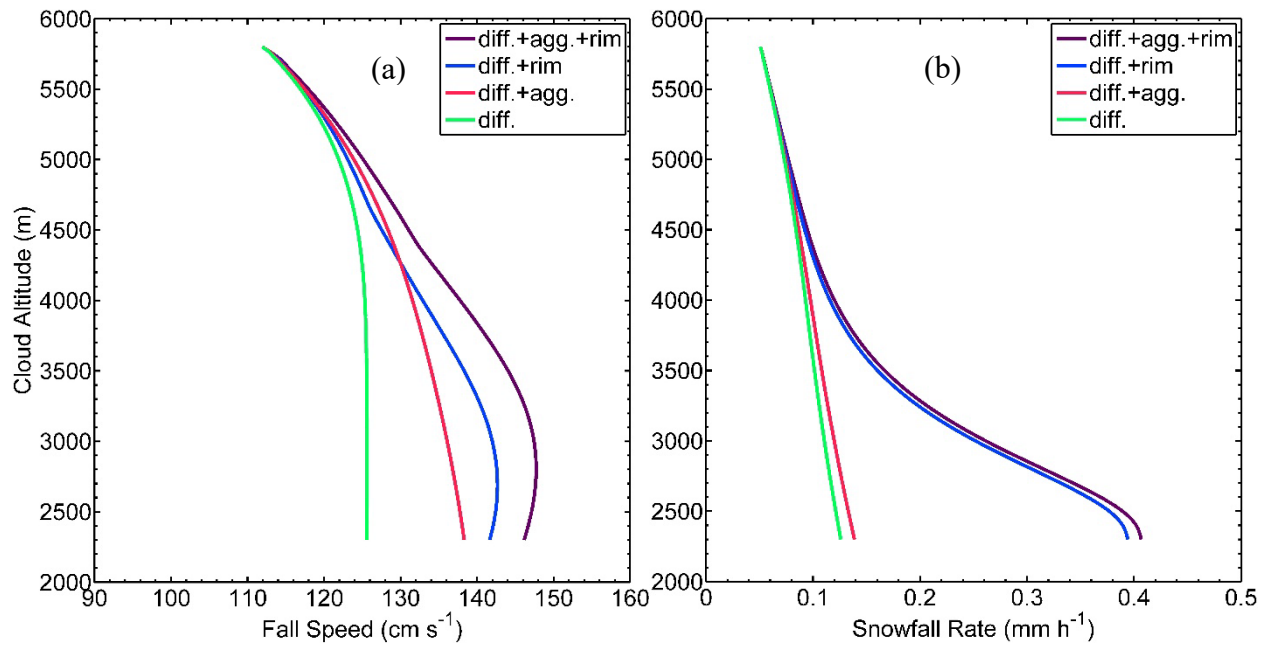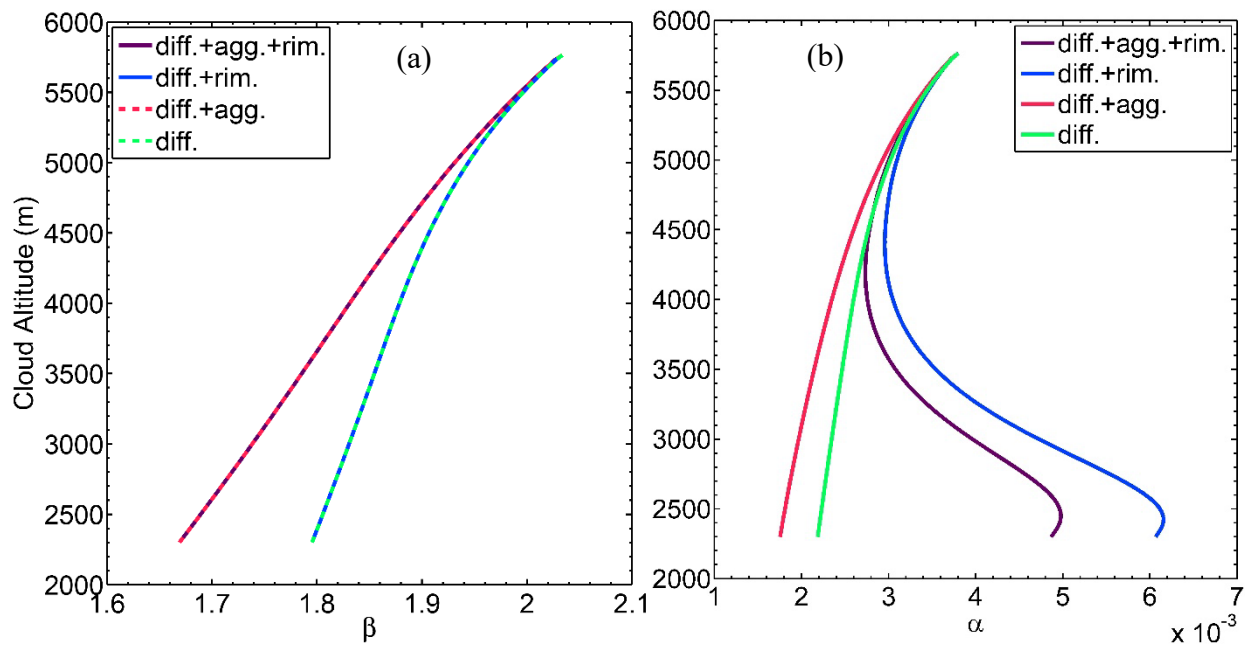
Figure 1. Vertical profile of liquid water content and relative humidity with respect to ice.

Figure 2. Vertical profile of (a) mean dimension, (b) number concentration, and (c) ice water content for various combinations of vapor diffusion, aggregation, and riming processes.

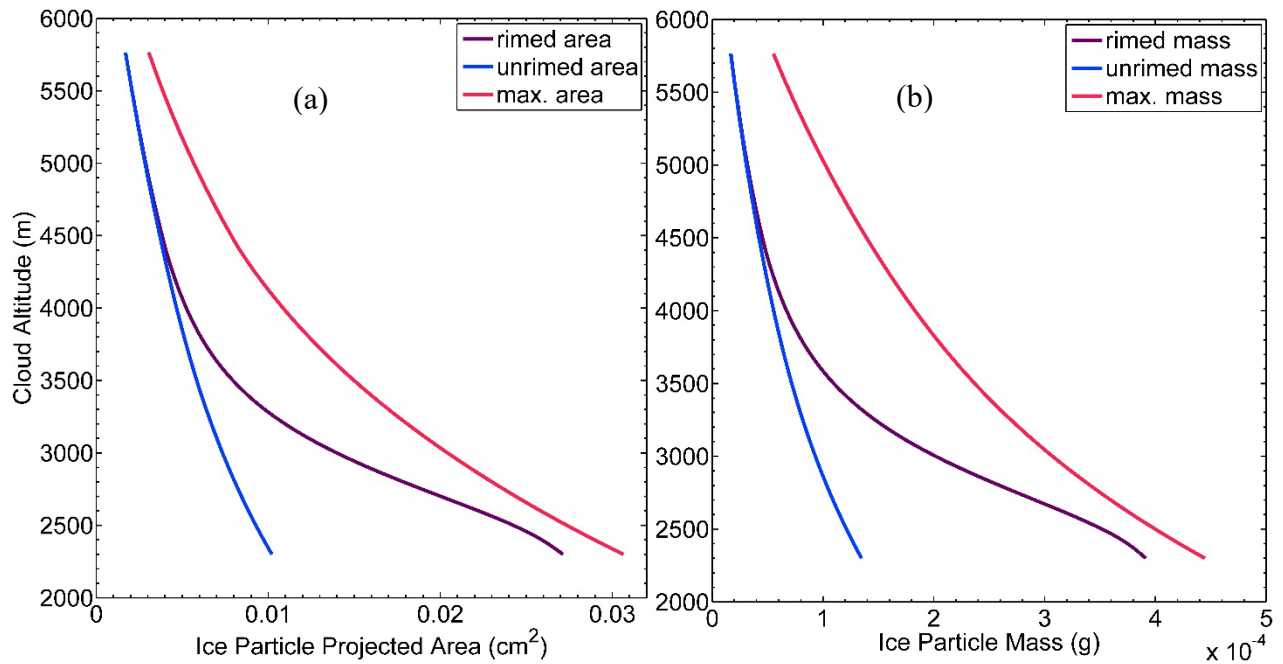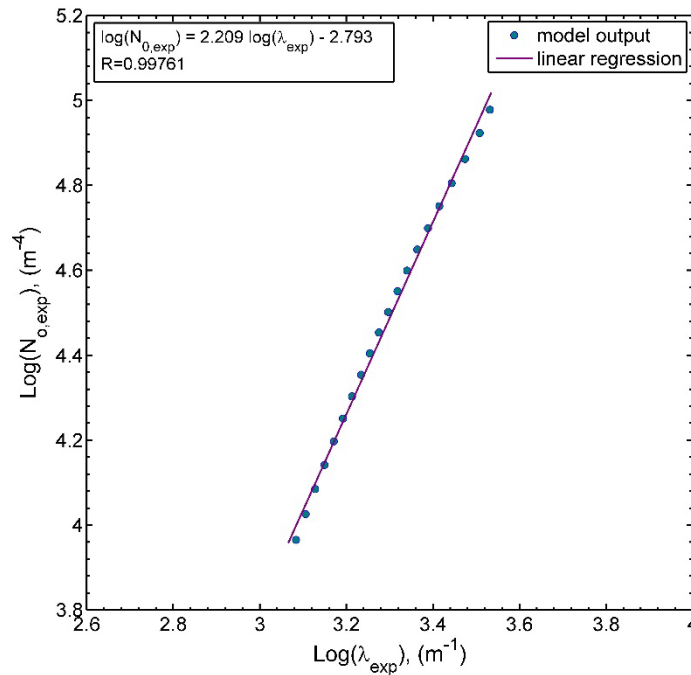Figure 3. Same as Fig. 2, but for (a) mass-weighted fallspeed and (b) snowfall rate.

705

Figure 4. Same as Fig. 3, but for (a) β and (b) α.

710　Figure 5. Vertical profile of (a) projected area and (b) mass calculated from median-mass dimension for rimed, unrimed, and graupel onset conditions (maximum mass and area refer to the graupel onset).

715　Figure 6. $\log(N_o)$ vs. $\log(\lambda)$ for exponential PSD. Each circle shows a vertical level in the modeled cloud with a vertical distance of 180 m to the upper or lower level. The cloud top is represented by the uppermost circle.

30

Figure 7. Vertical profile of snowfall rate for two liquid cloud PSDs: The blue curve corresponds to the drop median-mass diameter being equal to 10 μm, and the red curve represents the drop median-mass diameter being equal to 20 μm.
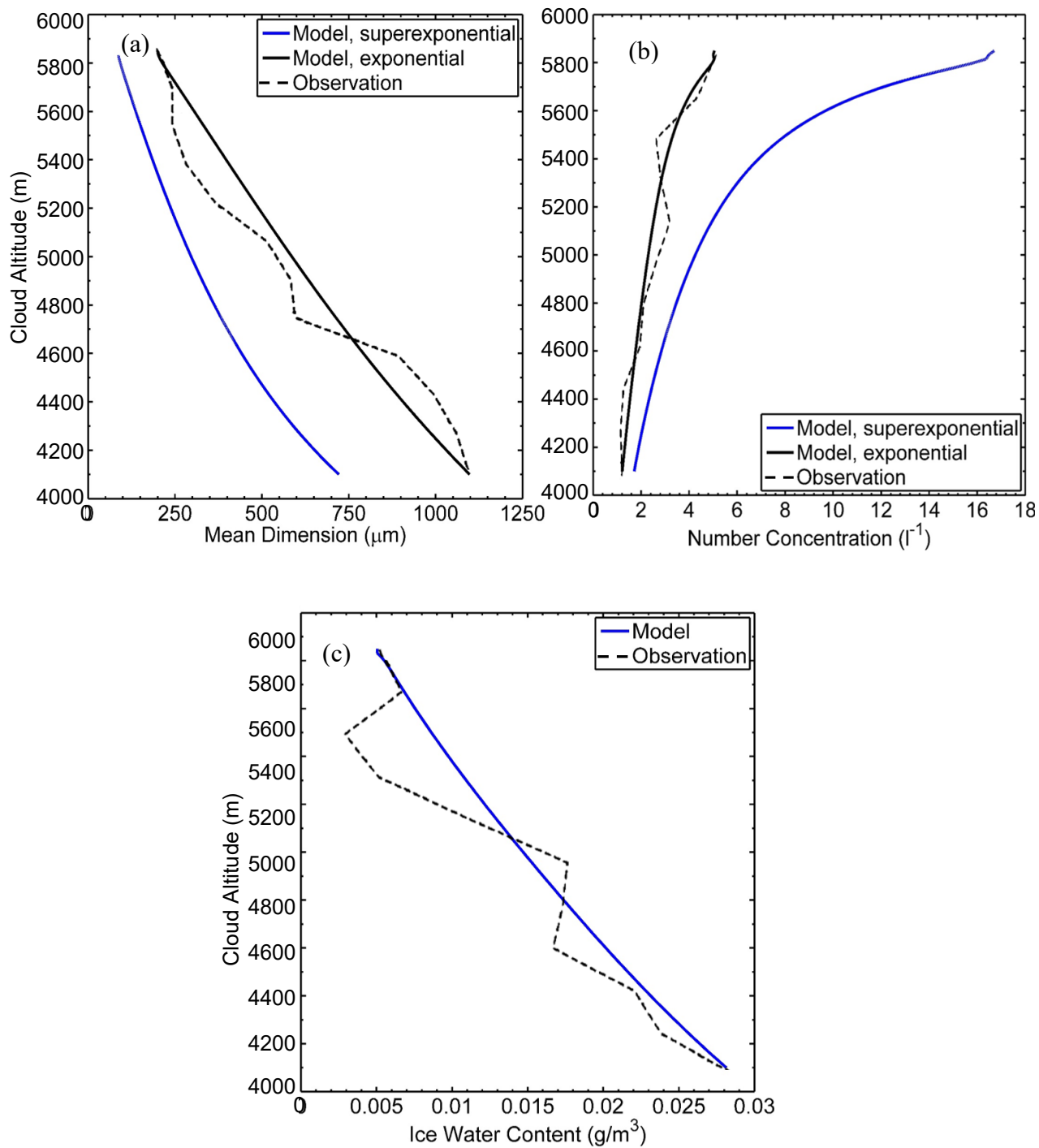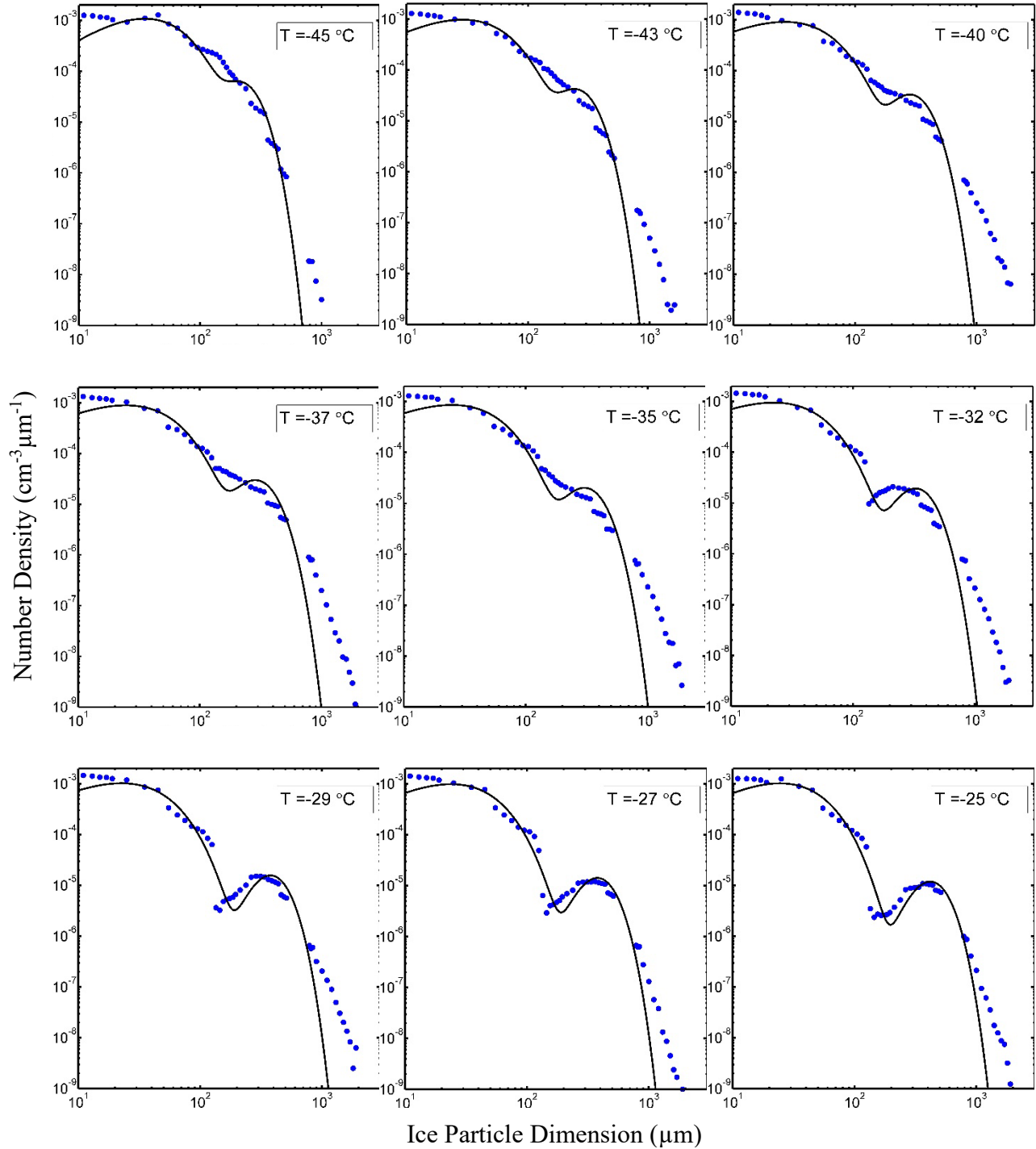
725

Figure 8. Vertical profile of (a) mean dimension and (b) number concentration for observation, model with super-exponential PSD, and model with exponential PSD. (c) Vertical profile of IWC for observation and model with exponential PSD. Observations are from Spiral 3.

Figure 9. Observed PSD (blue circles) and bimodal gamma PSD (black curves) fitted to the observed PSD. Observed PSD in each panel is provided by averaging a complete loop of the Lagrangian spiral. Observations are from flight B672.
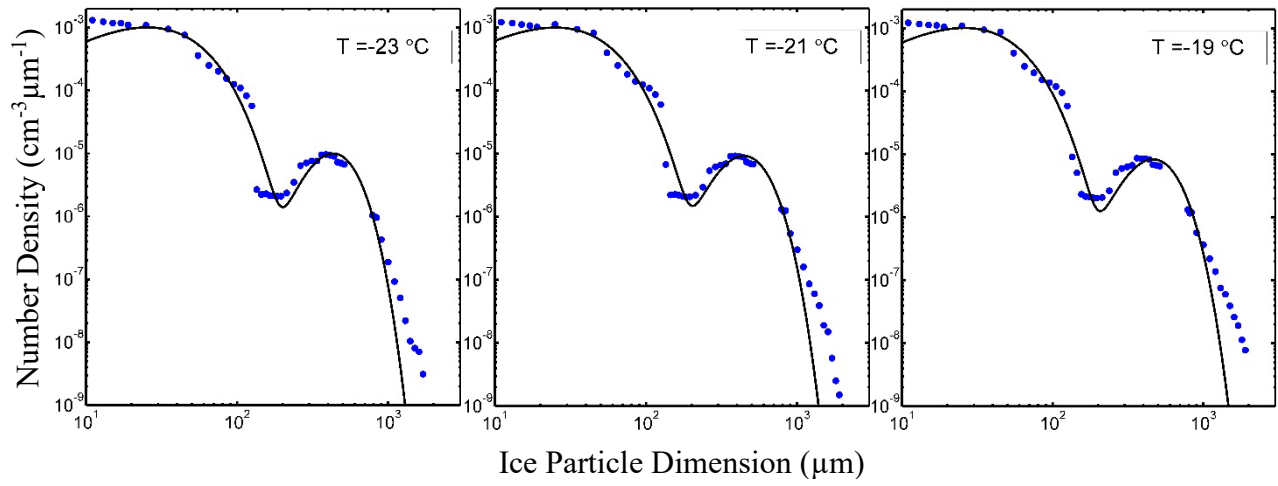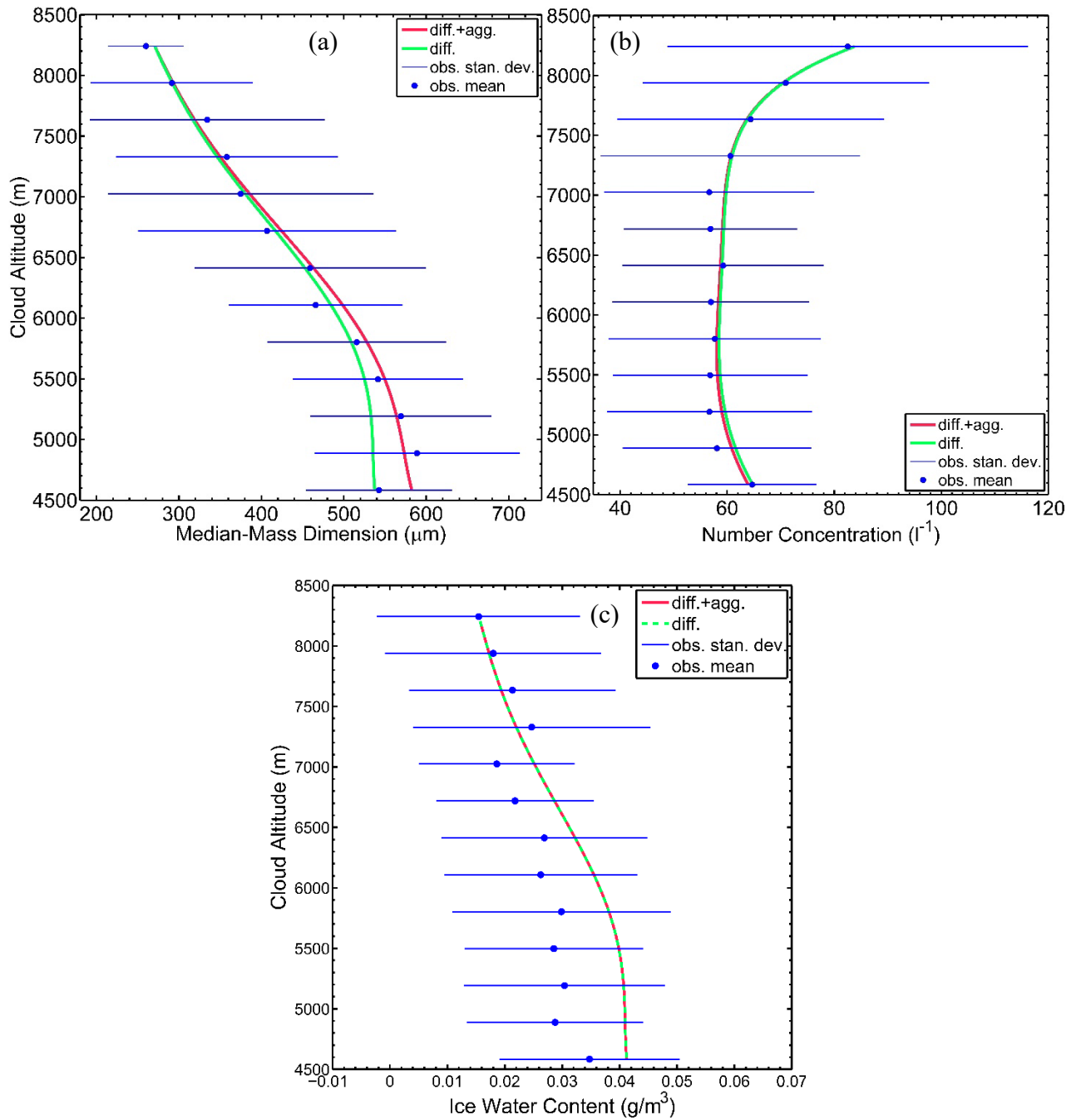
Figure 9. Continued.

740

Figure 10. Vertical profile of (a) median-mass dimension, (b) number concentration, and (c) ice water content for observation, model with diffusion and aggregation processes, and model with diffusion process. Each blue circle (horizontal line) is the mean (standard deviation) of a complete loop of the Lagrangian spiral. Observations are from flight B672.